The Astrophysical Journal, 786:51 (13pp), 2014 May 1 doi:10.1088/0004-637X/786/1/51

DETECTION OF COHERENT STRUCTURES IN PHOTOSPHERIC TURBULENT FLOWS

Abraham C.-L. Chian[1,2,3], Erico L. Rempel[1,4], Guillaume Aulanier[2], Brigitte Schmieder[2], Shawn C. Shadden[5], Brian T. Welsch[6], and Anthony R. Yeates[7]
[1] National Institute for Space Research (INPE), World Institute for Space Environment Research (WISER), P.O. Box 515, 12227-010 São José dos Campos-SP, Brazil; abraham.chian@gmail.com, rempel@ita.br
[2] Observatoire de Paris, LESIA, CNRS, F-92190 Meudon, France
[3] School of Mathematical Sciences, University of Adelaide, Adelaide, SA 5005, Australia
[4] Institute of Aeronautical Technology (ITA), WISER, 12228-900 São José dos Campos-SP, Brazil
[5] Department of Mechanical Engineering, University of California, Berkeley, CA 94720, USA
[6] Space Science Laboratory, University of California, Berkeley, CA 94720, USA
[7] Department of Mathematical Sciences, Durham University, Durham DH1 3LE, UK
Received 2013 December 7; accepted 2014 February 26; published 2014 April 16

ABSTRACT

We study coherent structures in solar photospheric flows in a plage in the vicinity of the active region AR 10930 using the horizontal velocity data derived from *Hinode*/Solar Optical Telescope magnetograms. Eulerian and Lagrangian coherent structures (LCSs) are detected by computing the Q-criterion and the finite-time Lyapunov exponents of the velocity field, respectively. Our analysis indicates that, on average, the deformation Eulerian coherent structures dominate over the vortical Eulerian coherent structures in the plage region. We demonstrate the correspondence of the network of high magnetic flux concentration to the attracting Lagrangian coherent structures (aLCSs) in the photospheric velocity based on both observations and numerical simulations. In addition, the computation of aLCS provides a measure of the local rate of contraction/expansion of the flow.

Key words: magnetohydrodynamics (MHD) – Sun: magnetic fields – Sun: photosphere – turbulence

Online-only material: color figures

1. INTRODUCTION

The spatiotemporal patterns and transport of magnetic field in the photosphere are driven by the turbulent plasma flows in the solar convection zone. Solar magnetic fields are observed in complex and hierarchical structures covering a wide range of scales that emerge and vanish on the timescales of turbulent convective patterns. Traditionally, they are classified by size and lifetime as patterns of granulation (1 Mm, 0.2 hr), mesogranulation (5–10 Mm, 5 hr), and supergranulation (15–35 Mm, 24 hr). Recently, the idea is emerging that meso- and supergranulation are signatures of a collective interaction of granular cells (Del Moro et al. 2007). The continuous restructuring of surface magnetic fields by photospheric turbulent flows plays a key role in determining the topology and evolution of chromospheric and coronal magnetic fields, and may influence the triggering of eruptive solar events such as flares, coronal mass ejections, or sudden disappearance of filaments (Roudier et al. 2009). For example, Rondi et al. (2007) and Roudier et al. (2008) used space- and ground-based observations to show that large-scale horizontal photospheric flows below and around a filament influence the formation and evolution of filaments, leading to destabilization of the coronal magnetic field.

Spectral line observations of the Sun with high spatial resolution show small-scale bright points, with widths $\lesssim 0.5$ Mm, located in the intergranular lanes. Bright points are associated with localized regions of strong magnetic field and correspond to magnetic flux tubes of kilogauss field strength that stand nearly vertically in the solar atmosphere (Solanki 1993). Some bright points exhibit the proper motions of convectively driven vortical flows created at the downdrafts where the plasma follows spiral paths and returns to the solar interior after cooling down (Bonet et al. 2008). Recent balloon-borne Sunrise observations show 3.1×10^{-3} vortices Mm^{-2} minute^{-1}, with a mean lifetime of 7.9 minutes and a standard deviation of 3.2 minutes (Bonet et al. 2010). These magnetized vortex tubes have been predicted by the theory of magnetoconvection (Brandenburg et al. 1996; Stein & Nordlund 1998) and observed in three-dimensional (3D) radiative/compressible MHD simulations (Kitiashvili et al. 2010, 2012; Shelyag et al. 2011; Rempel et al. 2013). Photospheric vortex structures with high concentration of magnetic field provide an important path for energy and momentum transfer from the convection zone into the chromosphere (Kitiashvili et al. 2012) and may be relevant for chromospheric-coronal heating (van Ballegooijen et al. 1998; Hasan & van Ballegooijen 2008).

A number of observational and theoretical works have applied the Lagrangian approach to trace the flow of bright points and the pattern of the magnetic network. Simon et al. (1988) measured the horizontal flow field on the solar surface using the technique of local correlation tracking (LCT) on a 28 minute time sequence of white-light images of the Solar Optical Universal Polarimeter instrument on board *Spacelab2*. They showed that insight into the relationship between flows and magnetic fields is acquired by calculating the flow of passive test particles, called "corks," that are originally distributed uniformly in the flow field. The cork paths, representing the Lagrangian tracers of the path lines of the flow, congregate at the same locations of the magnetic network. A simplified kinematic model of convection at the solar surface was developed by Simon & Weiss (1989) to interpret observations and predict the evolution of magnetic fields. They compared the cork patterns of the simulated flow with the cork patterns of the observed magnetic network and discussed the extent to which magnetic flux tubes can be regarded as moving passively with the large-scale photospheric flow. van Ballegooijen et al. (1998) used the G-band images of the Swedish Vacuum Solar Telescope to show that bright points are arranged in linear structures, called "filigrees," located in the lanes between neighboring granule cells, and to measure the motion of bright points using an object tracking technique;

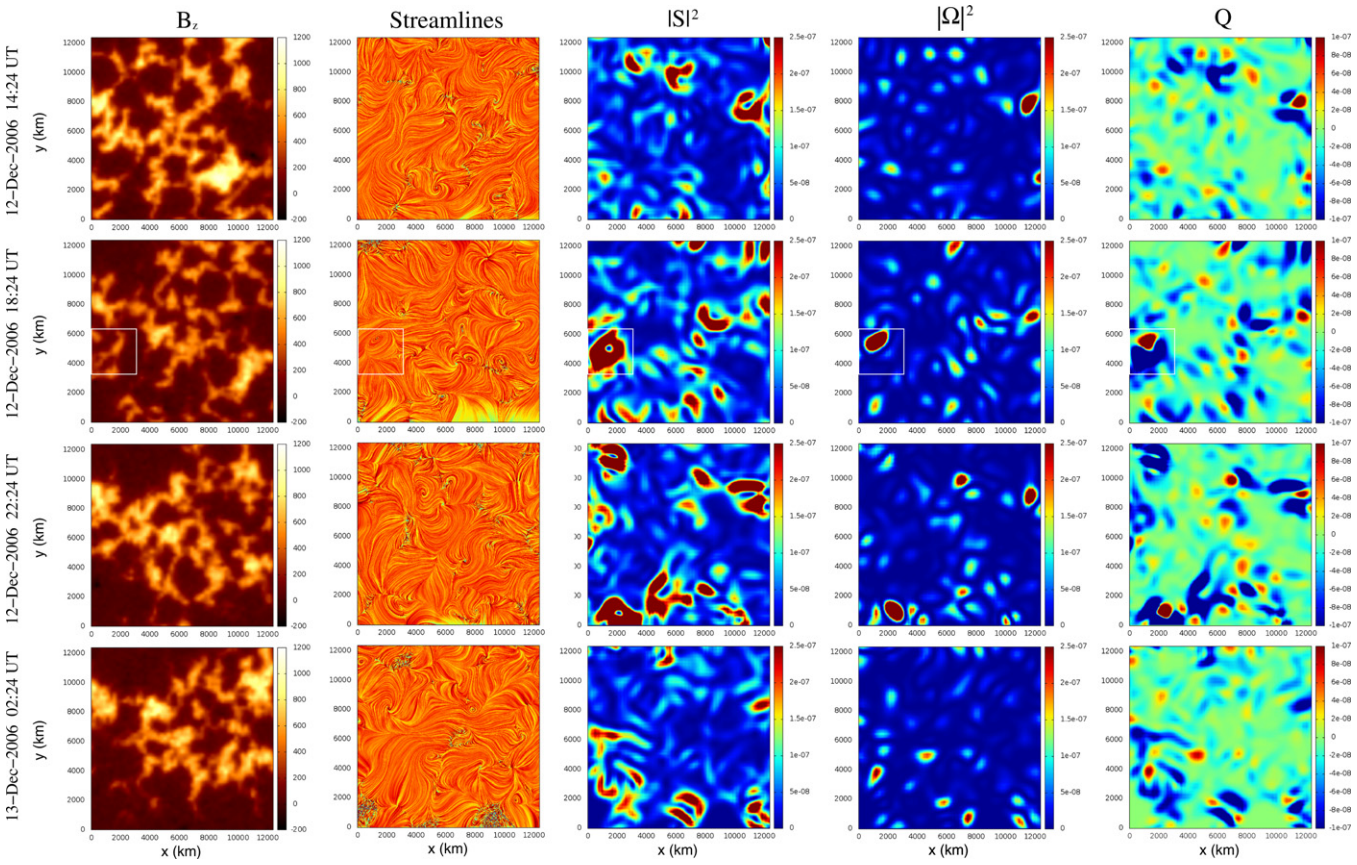

Figure 1. Images of the magnetic field $B_z(G)$, streamlines, deformation (S), and vortical (Ω) Eulerian coherent structures, and Q-criterion Q at 2006 December 12 14:24 UT, 2006 December 12 18:24 UT, 2006 December 12 22:24 UT, 2006 December 13 02:24 UT (from top to bottom).

(A color version of this figure is available in the online journal.)

comparison with a two-dimensional (2D) simulation of horizontal motions of magnetic flux elements in response to solar granulation flows shows that the observed velocities and spatial distribution of the bright points are consistent with passive advection of corks by the solar granulation flow. Del Moro et al. (2007) used the IBIS spectrometer and cork technique to study the 3D velocity field of a supergranular cell at two photospheric heights and showed that strong converging downflows occur at the boundary of the supergranular cell that is cospatial with clusters of magnetic network, whereas compact diverging upflows occur near the center of the supergranular cell. Schmieder et al. (2013) applied the coherent structure tracking algorithm to track granules and analyze large-scale photospheric flows related to an extended filament in the active region AR 11106 using the H_α imager of the THEMIS telescope and the EUV imager (AIA) of Solar Dynamic Observatory. They showed that diverging flows inside the supergranules may be similar in and out of the filament channel. In addition, they identify converging flows, corresponding to accumulation of corks, around the footpoints or barbs located at the edges of the EUV filament. The frequent EUV brightenings suggest the occurrence of reconnections of the magnetic field lines of the flux tube with the environment at the convergence points at the edges of the EUV filament channel.

There is observational evidence of anomalous transport and turbulence in photospheric flows and magnetic fields. Schrijver et al. (1992) and Lawrence & Schrijver (1993) applied the percolation theory to report sub-diffusion of magnetic elements in the photosphere. Cadavid et al. (1999) used a 70 minute sequence of G-band images of the Swedish Vacuum Solar Telescope on 1995 October 5 to show that the transport of bright points near the disk center is sub-diffusive due to the trapping of walkers at the stagnation points in the fractal intercellular pattern; the distribution of waiting times at the trap sites obeys a Lévy (power-law) distribution. Lawrence et al. (2001) applied subsonic filtering to the data of Cadavid et al. (1999) to report super-diffusion and show that the spatiotemporal scaling of the bright point dynamics indeed indicates the presence of turbulence in the intergranular lanes. Lawrence et al. (2011) studied the G-band high-frequency fluctuations at the photosphere and chromosphere using the Rapid Oscillations in the Solar Atmosphere instrument of the Dunn Solar Telescope. They showed that the power spectra of high-frequency oscillations display a scale-invariant behavior with a spectral index indicative of nonlinear chaotic or turbulent processes, different from white noise or Brownian motion. In addition, they observed concentrations of magnetic bright points in the intergranular lanes that are associated with intermittent high-frequency fluctuations characterized by a positive kurtosis, implying non-Gaussian pdfs typical of turbulence. Their observations render support for the model proposed by Hasan & van Ballegooijen (2008), whereby high-frequency magnetoacoustic waves are produced by the interaction of magnetic flux tubes with turbulent downflows in the intergranular lanes. Cadavid et al. (2012) showed that the noise-filtered power spectrum of the *Hinode*/Solar Optical Telescope (SOT) data with a sequence of 80 minutes on 2007 March 5, in the internetwork near the Sun center of size 20 Mm × 20 Mm, presents a scaling range of $32 < f < 53$ MHz with characteristic power-law exponents of -1.56 for G band and of -4.00 for H line, confirming the presence of turbulent fluctuations. By integrating

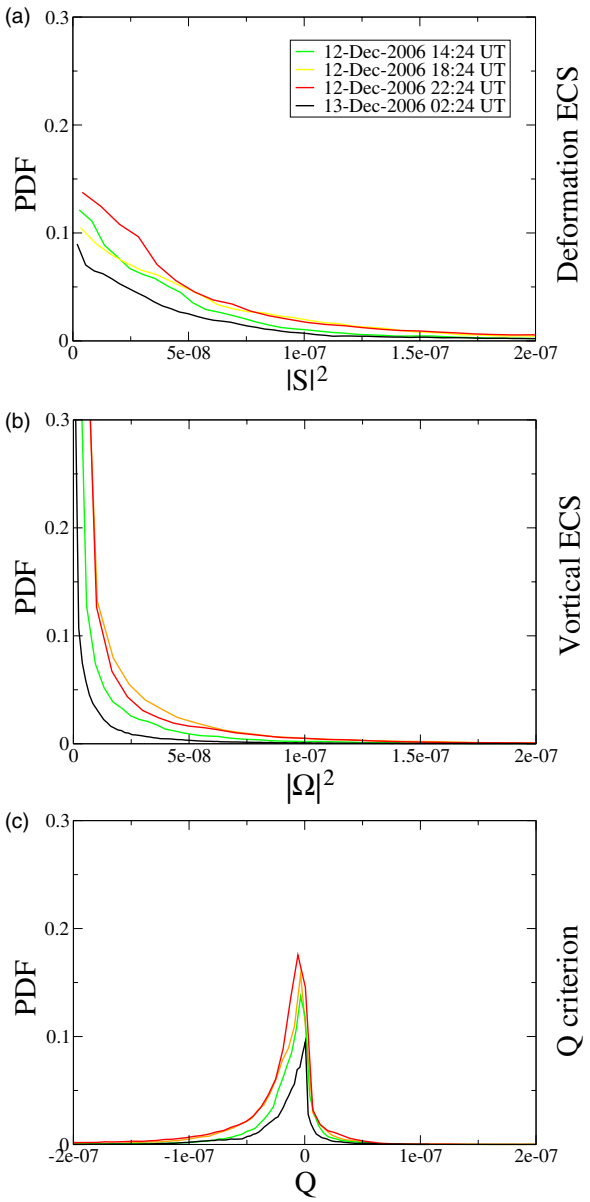

Figure 2. pdf of Eulerian coherent structures as a function of (a) $|S|^2$, (b) $|\Omega|^2$, and (c) Q-criterion, at 2006 December 12 14:24 UT (green), 2006 December 12 18:24 UT (yellow), 2006 December 12 22:24 UT (red), and 2006 December 13 02:24 UT (black).

(A color version of this figure is available in the online journal.)

the *Hinode*/SOT G-band spectra in the range 32–53 MHz, they identified the sites of increased G-band power with the location of G-band bright points. Abramenko et al. (2011) and Lepreti et al. (2012) used the images of the New Solar Telescope of Big Bear Solar Observatory to report super-diffusion and turbulent pair dispersion of bright points in the active region plage, quiet Sun, and coronal hole.

The aim of this paper is to apply Eulerian and Lagrangian tools to detect coherent structures in images of photospheric turbulent flows. First, we apply the Eulerian approach to compute the Q-criterion and distinguish regions of the plasma flow dominated by the deformation and vortical coherent structures (Hunt et al. 1988). Next, we apply the tool of Lagrangian coherent structures to determine the repelling and attracting material lines that organize the transport of plasma flow. The term "Lagrangian" refers to flows defined by the fluid motion instead of an instantaneous snapshot (Eulerian); the term "coherent" refers to the distinguished stability of these structures compared to other nearby material lines/surfaces. There is a growing interest to adopt the LCS approach (Haller & Yuan 2000; Shadden 2011) to improve the understanding of transport in complex flows such as planetary atmosphere (Sapsis & Haller 2009; Peng & Peterson 2012), oceans (Beron-Vera et al. 2010; Lehahn et al. 2011), and the cardiovascular system (Shadden & Taylor 2008; Arzani & Shadden 2012). A number of papers have studied LCS in complex plasma flows for thermonuclear applications (Leoncini et al. 2006; Padberg et al. 2007; Borgogno et al. 2011) and astrophysical applications (Rempel et al. 2011, 2012, 2013; Yeates et al. 2012). In this paper, we apply the backward finite-time Lyapunov exponents (b-FTLEs) to study the attracting LCS of the photospheric turbulence. We show that, like the "corks," the b-FTLE is able to trace the patterns of the magnetic network. Moreover, it gives a quantitative measure of the local rate of contraction/expansion of the photospheric flow.

2. THE HORIZONTAL VELOCITY DATA

Our study is based on a 12 hr high-resolution sequence of velocity images (cadence ∼121 s) of photospheric flow derived from the *Hinode*/SOT magnetograms, from 2006 December 12 14:24 UT to 2006 December 13 02:24 UT, by selecting a unipolar plage area of size 12.4 Mm × 12.4 Mm (∼17″ × 17″) near the active region AR 10930 (Yeates et al. 2012). The horizontal velocity field is a "proxy" extracted from the line-of-sight magnetic field (B_z) using the Fourier LCT method (FLCT; Welsch et al. 2004, 2012).

It is worth pointing out that there are uncertainties in the correlation tracking that do not fully resolve the velocity fields in either space or time. The detailed description of the data reduction procedure is given in Welsch et al. (2012) and Yeates et al. (2012). The FLCT method involves a number of optimum parameters that are determined by an autocorrelation analysis in order to maximize frame-to-frame correlations and ensure robustness in the velocity estimate. In view of the reduction of noise by averaging in the tracking procedure, the actual velocity patterns of the photospheric flow might be more complicated than the "proxy."

Yeates et al. (2012) proposed a direct method to obtain the time-dependent buildup of magnetic structures in the solar corona by integrating a time sequence of observed horizontal velocity fields in the solar photosphere, which offers advantages over the indirect method of extrapolating the coronal magnetic field from photospheric magnetograms. In particular, they showed that the quasi-separatrix layers (Démoulin et al. 1996) in the coronal magnetic field correspond to the repelling LCS in the photospheric flow. In this paper, we extend the analysis of Yeates et al. (2012) to establish the correspondence of the network of high magnetic flux concentration to the aLCS in the photospheric velocity.

3. EULERIAN COHERENT STRUCTURES IN THE PHOTOSPHERE

Eulerian coherent structures can be extracted from the velocity field by computing the Q-criterion, also known as the Okubo–Weiss parameter in 2D turbulence (Hunt et al. 1988),

$$Q = \frac{1}{2}[|\Omega|^2 - |S|^2], \quad (1)$$

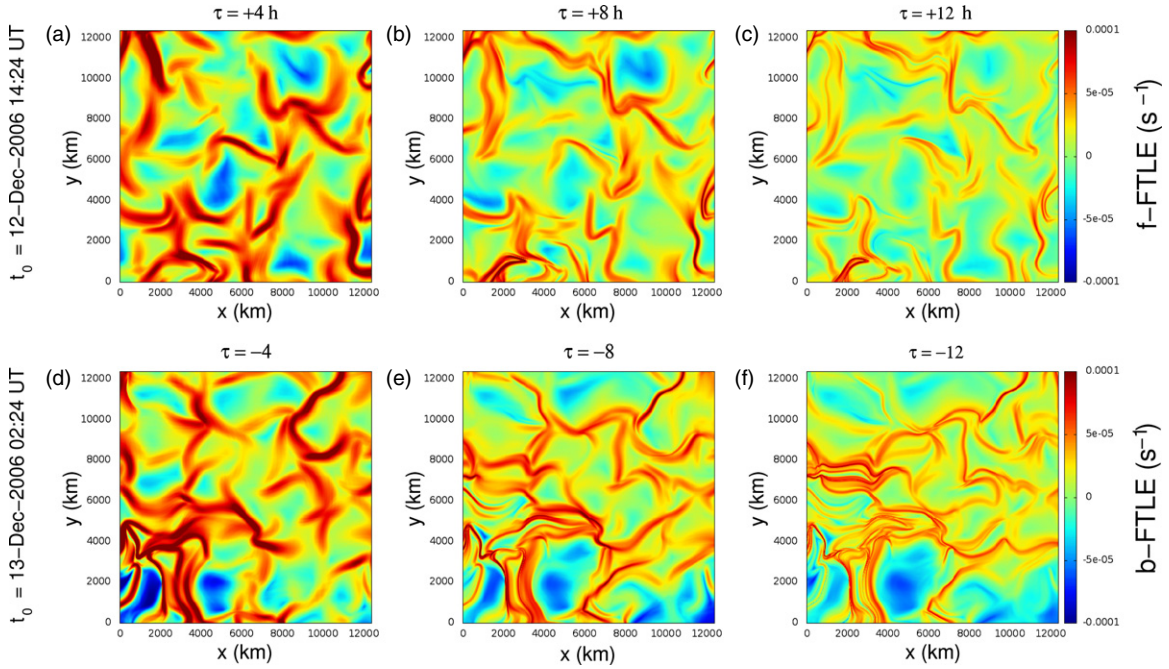

Figure 3. Lagrangian coherent structures. Upper panel: f-FTLE for t_0 at 2006 December 12 14:24 UT with (a) $\tau = +4$ hr, (b) $\tau = +8$ hr, and (c) $\tau = +12$ hr. Bottom panel: b-FTLE for t_0 at 2006 December 13 02:24 UT with (d) $\tau = -4$ hr, (e) $\tau = -8$ hr, and (f) $\tau = -12$ hr.

(A color version of this figure is available in the online journal.)

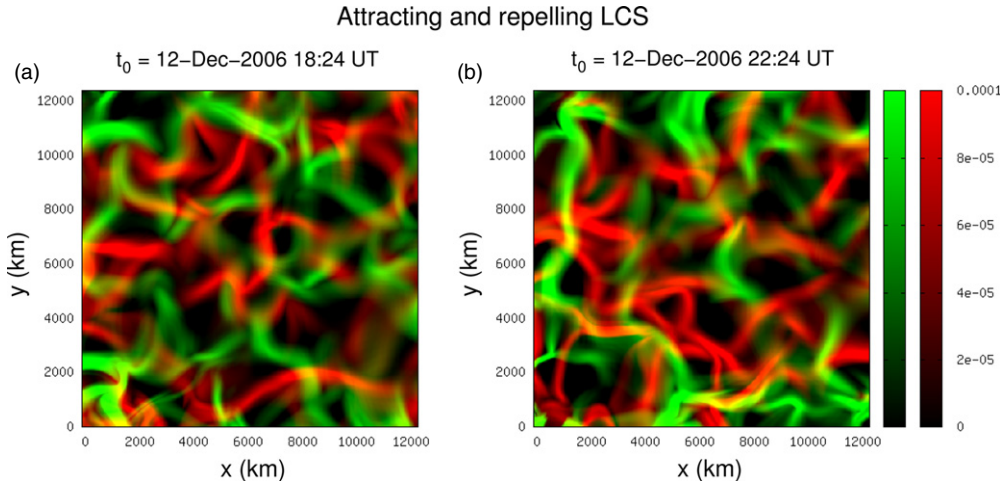

Figure 4. Attracting and repelling Lagrangian coherent structures given, respectively, by the b-FTLE (s^{-1}) (red) and f-FTLE (s^{-1}) (green) at (a) 2006 December 12 18:24 UT and (b) 2006 December 12 22:24 UT.

(A color version of this figure is available in the online journal.)

where the Frobenius matrix norm is adopted and S and Ω are defined by the decompositions of the gradient tensor of the velocity field

$$\nabla u = S + \Omega, \tag{2}$$

and

$$S = \frac{1}{2}[\nabla u + (\nabla u)^{\top}], \quad \Omega = \frac{1}{2}[\nabla u - (\nabla u)^{\top}], \tag{3}$$

where $\top$ denotes the transpose of a tensor. The strain-rate (or deformation) tensor S is the symmetric part of ∇u; its eigenvectors form an orthonormal set along the principle directions of fluid element deformation caused by tension, and its eigenvalues are real quantities that measure the rates of deformation in the corresponding directions. The vorticity tensor Ω is the antisymmetric part of ∇u. For example, the deformation calculated using the *Ulysses* data shows that the magnetic tension causes local stretching of solar wind plasma elements mostly along the direction of the average magnetic field, whereas the solar wind vorticity tends to become perpendicular to the mean radial direction at large heliospheric distances (Polygiannakis et al. 1996).

Snapshot images of Eulerian coherent structures of the horizontal velocity field detected by *Hinode* in a plage region near AR 10930 (Yeates et al. 2012) are shown in Figure 1 for four instances: 2006 December 12 14:24 UT, 2006 December 12 18:24 UT, 2006 December 12 22:24 UT, 2006 December 13 02:24 UT. The first column shows magnetograms;

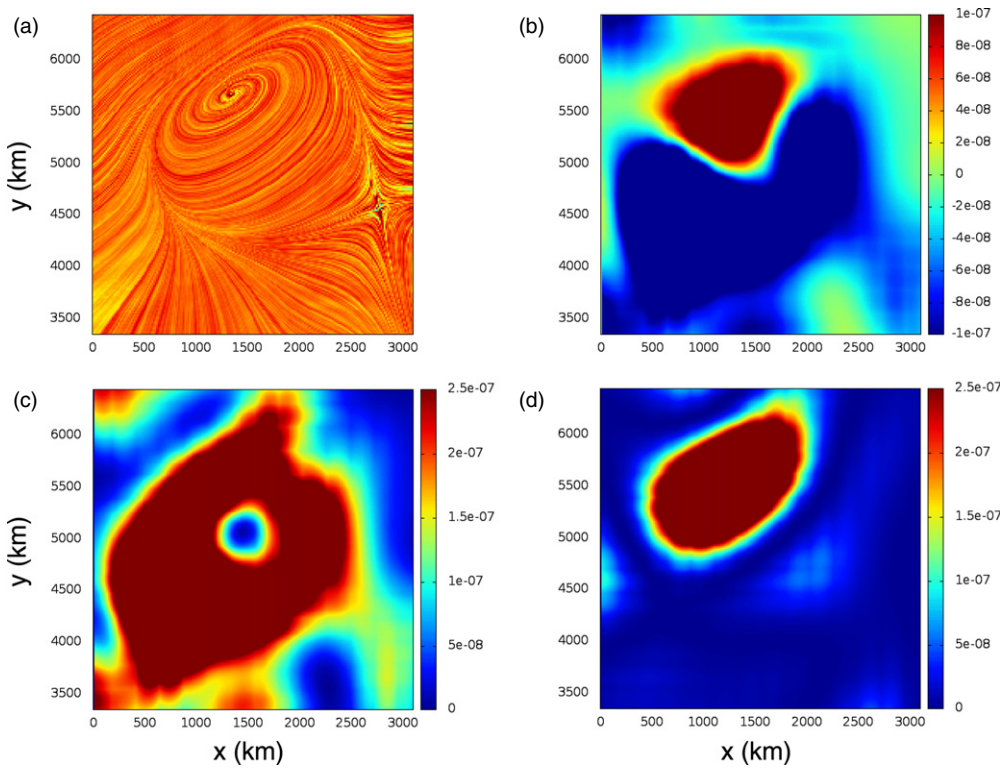

Figure 5. Enlargement of the rectangle region indicated in Figure 1 at 2006 December 12 18:24 UT: (a) streamlines, (b) Q-criterion, (c) $|\Omega|^2$, and (d) $|S|^2$. (A color version of this figure is available in the online journal.)

the second column depicts the streamlines computed using the method of line integral convolution, which displays the integral curves of (u_x, u_y) in different tones of orange; some vortex coherent structures (patches) can be visualized in these plots. The third column depicts the (x, y) plots of the deformation Eulerian coherent structures, which are identified by the localized patches with high values of $|S|^2$. The fourth column depicts the (x, y) plots of the vortical Eulerian coherent structures, which are identified by the localized patches with high values of $|\Omega|^2$. The average spatial size and lifetime of these vortices are similar to the magnetic bright points observed by Bonet et al. (2008, 2010). The fifth column depicts the (x, y) plots of the Q-criterion given by Equation (1), which partitions the turbulent flow into the deformation-dominated ($Q < 0$, blue patches) and vorticity-dominated ($Q > 0$, red patches) regions.

The intensity of a turbulent flow is characterized by the magnitude of the rms velocity fluctuations, deformation, and vorticity (Steinberg & Driscoll 2009). The pdfs of Eulerian coherent structures (ECS), associated with Figure 1, are shown in Figure 2. Some trends are evident. Figures 2(a) and (b) show that there are higher (lower) statistics for the low (high) values of the magnitudes of deformation and vorticity. Figure 1(c) shows that for all four instances the Q-criterion is distributed among negative and positive values, with non-Gaussian pdf. Note that the pdf of the Q-criterion shows a strong asymmetry skewed toward negative values, which indicates that in the plage region under study the photospheric turbulent flow is dominated by the strain-rate field. This situation is similar to a laboratory experiment of the turbulence-flame interaction, where the flame surface straining is dominated by the deformation whereas the role of the vorticity is to curve the flame surface, creating wrinkles (Steinberg & Driscoll 2009).

Table 1
Mean Values of the Eulerian Coherent Structures

	$\langle\|S\|^2\rangle$	$\langle\|\Omega\|^2\rangle$	$\langle Q\rangle$
2006 Dec 12 14:24 UT	$5.0453e{-}08$	$1.8139e{-}08$	$-1.6157e{-}08$
2006 Dec 12 18:24 UT	$7.3680e{-}08$	$2.4142e{-}08$	$-2.4769e{-}08$
2006 Dec 12 22:24 UT	$8.0154e{-}08$	$2.2815e{-}08$	$-2.8670e{-}08$
2006 Dec 13 02:24 UT	$4.9614e{-}08$	$1.4840e{-}08$	$-1.7387e{-}08$

The mean values of Eulerian coherent structures for four instances are summarized in Table 1. It confirms the features of pdf seen in Figure 2, i.e., in the plage region under study, on average: (1) the deformation dominates over the vorticity, and (2) the Q-criterion shows negative values, implying the dominance of the deformation coherent structures over the vortical coherent structures.

Although the deformation and vortical coherent structures can be extracted by the Eulerian technique using the Q-criterion, it relies on instantaneous snapshots of the velocity field. In the next section we show that the transport barriers in the turbulent flow can be detected with greater precision by the technique of LCS.

4. LAGRANGIAN COHERENT STRUCTURES IN THE PHOTOSPHERE

Analogous to "corks" discussed in Section 1, the finite-time Lyapunov exponent (FTLE) can be computed by advecting a dense grid of tracer particles over the domain of interest. Consider a passive particle advected by the velocity field $\mathbf{u}(\mathbf{r}, t)$ from an initial time t_0. We use the horizontal velocity field derived from the *Hinode*/SOT data for the plage region of

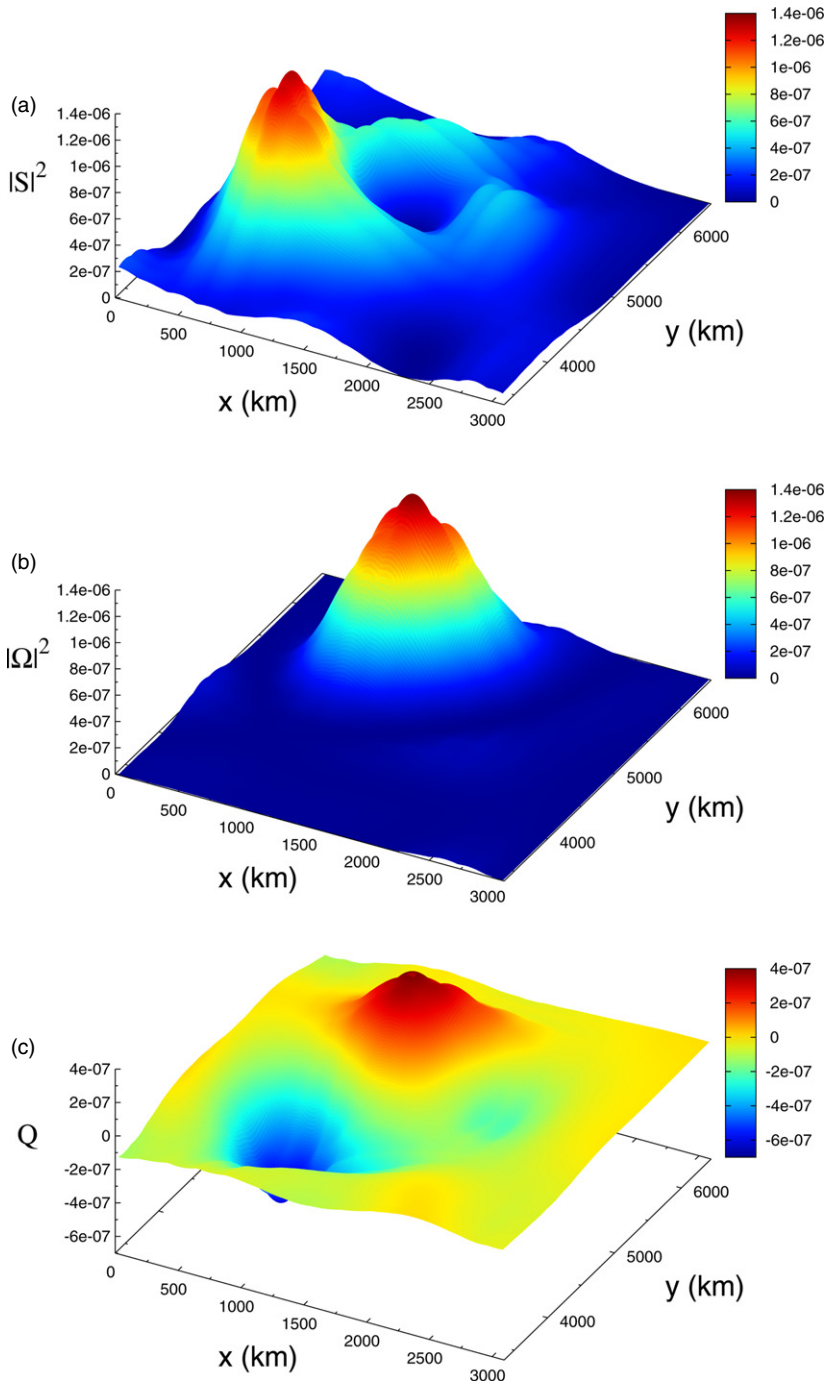

Figure 6. 3D plots of Eulerian coherent structures as a function of (x, y), corresponding to Figure 5. (a) $|S|^2$, (b) $|\Omega|^2$, and (c) Q-criterion. (A color version of this figure is available in the online journal.)

Figure 1 to solve the particle advection equation

$$\frac{d\mathbf{r}}{dt} = \mathbf{u}(\mathbf{r}, t), \quad \mathbf{r}(t_0) = \mathbf{r}_0, \tag{4}$$

over a grid of initial positions $\mathbf{r}_0$ until the final positions $\mathbf{r}(t_0 + \tau)$ are reached after a finite integration time τ. The particle trajectories are obtained by a fourth-order Runge–Kutta integrator with cubic spline interpolation in both space and time. The FTLEs of the particle trajectories for a 2D flow are calculated at each initial position $\mathbf{r}_0$ as (Shadden et al. 2005; Shadden 2011; Rempel et al. 2011, 2012, 2013; Yeates et al. 2012)

$$\sigma_i^{t_0+\tau}(\mathbf{r}_0) = \frac{1}{|\tau|} \ln \sqrt{\lambda_i}, \quad i = 1, 2, \tag{5}$$

where λ_i ($\lambda_1 > \lambda_2$) are the eigenvalues of the finite-time right Cauchy–Green deformation tensor $\Delta = J^\top J$, $J = d\phi_{t_0}^{t_0+\tau}(\mathbf{r})/d\mathbf{r}$ is the deformation gradient, $\top$ denotes the transpose, and $\phi_{t_0}^{t_0+\tau} : \mathbf{r}(t_0) \rightarrow \mathbf{r}(t_0 + \tau)$ is the flow map for Equation (4). In forward time ($\tau > 0$), the maximum FTLE, σ_1, gives the finite-time average of the maximum rate of either divergence (if $\sigma_1 > 0$) or convergence (if $\sigma_1 < 0$) between the trajectories

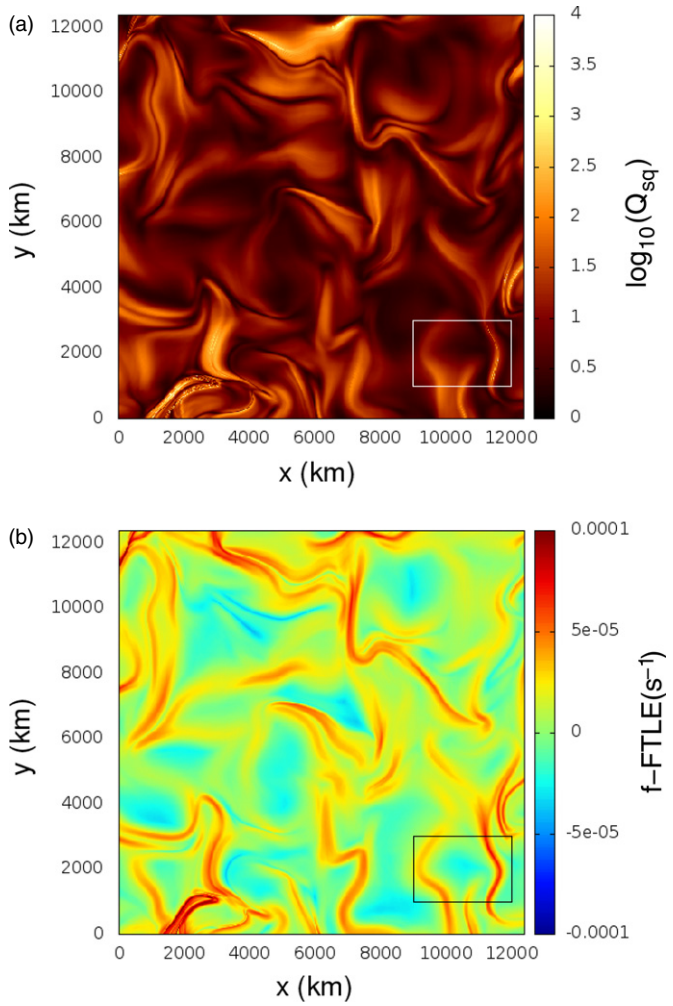

Figure 7. Comparison of the squashing Q-factor and repelling LCS. (a) Intensity plot of $\log_{10}(Q_{sq})$; (b) f-FTLE for $t_0 =$ 2006 December 12 14:24 UT and $\tau =$ +12 hr.

(A color version of this figure is available in the online journal.)

of a fiducial particle at $\mathbf{r}$ and its neighboring particles. The maximum stretching is found when the neighboring particle $\mathbf{s}$ is such that $\xi_0 = \mathbf{r}_0 - \mathbf{s}$ is initially aligned with the eigenvector of Δ associated with λ_1. If two points are initially separated by a small distance $|\xi_0|$ at time t_0, then their maximum separation at a later time t_1 will be $|\xi_1| \sim \exp[\sigma_1^{t_1}(\mathbf{r}_0)|t_1 - t_0|]|\xi_0|$. σ_2 provides information about stretching/contraction in another direction and can be useful to interpret the local dynamics of the fluid. Local minima in the maximum forward finite-time Lyapunov exponent (f-FTLE) provide a way to detect the position of the center of vortices in the velocity field since vortices may be viewed as material tubes of low particle dispersion. In backward time ($\tau < 0$), $\sigma_1 > 0$ represents regions of the flow with convergence and $\sigma_1 < 0$, regions with divergence of nearby trajectories.

The spectrum of σ_i given by Equation (5) does not put a practical limit on the integration time τ in the FTLE. λ_i are singular values of the deformation gradient matrix and are always positive. Contraction/expansion in direction i is related to whether λ_i is greater or less than 1, i.e., whether σ_i is greater or less than 0. When the flow is volume preserving, then the product must be 1 and one only gets one spectrum type, $\lambda_2 < 1 < \lambda_1$. If the flow is not volume preserving (as in our case), three different situations for the signs of σ_1, σ_2 may take place, ++, +−, and − −, leading to an expanding ellipse, collapse in one direction, or collapse in both directions, respectively. Here we note that collapse in one direction is the predominant situation, although we have regions where expanding ellipses or collapse in both directions are seen. The appropriate choice of τ depends on what timescale one is interested in. For example, Yeates et al. (2012) looked at the accumulated "braided" structures that the footpoint motions would produce in the coronal magnetic field. Hence, they took quite long integration times. On the other hand, they found that, since the flow has a large diverging component, the overall pattern tends to "set in" rather quickly as trajectories initially separate. Once separated, they become uncorrelated, and no completely new coherent structures arise if the integration is continued for longer. Rather, the existing ones gradually fragment, as seen in Figure 3. If, instead, one restarts the integration at a later time, one would see a different pattern corresponding to the convection cells present at that later time. Hence, the practical "lower limit" of τ might be the time taken for this basic pattern to set in (comparable to the granular or supergranular cell-crossing time).

Advecting a particle forward in time reveals the repelling LCS in the f-FTLE field, which is the source of stretching in the flow, whereas advecting a particle backward in time reveals the aLCS in the b-FTLE field along which particles congregate to form the observable patterns (Sapsis & Haller 2009). The properties of an LCS depend on the choice of the integration time τ, which should be chosen long enough for dominant features to be revealed, yet short enough for the FTLE to be representative of the transient dynamics of interest.

Three examples of repelling LCS for the photospheric turbulent flow in the plage region under study are given in Figures 3(a)–(c), which show the maximum f-FTLE σ_1 computed by solving the particle advection Equation (4) from the initial time $t_0 =$ 2006 December 12 14:24 UT to the final time $t_0 + \tau$, with $\tau =$ +4 hr (Figure 3(a)), +8 hr (Figure 3(b)), and +12 hr (Figure 3(c)), respectively. Thin ridges of large (positive) f-FTLE in Figures 3(a)–(c) represent the locally strongest repelling material lines in the photospheric flow, which confirm the results of Yeates et al. (2012) using $\tau =$ +6 hr and +12 hr. As we increase integration time, we notice that some structures persist and become more sharply defined. These structures can be considered most influential over time. The structures that fail to persist as integration time is increased can be considered to be due to more transient flow features.

Three examples of aLCS for the photospheric turbulent flow in the plage region under study are given in Figures 3(d)–(f), which show the maximum b-FTLE σ_1 computed by solving the particle advection Equation (4) from the initial time $t_0 =$ 2006 December 13 02:24 UT to the final time $t_0 + \tau$, with $\tau = -4$ hr (Figure 3(d)), −8 hr (Figure 3(e)), and −12 hr (Figure 3(f)), respectively. Thin ridges of large (positive) b-FTLE in Figures 3(d)–(f) represent the locally strongest attracting material lines in the photospheric flow.

In order to illustrate the temporal evolution of LCS, we compute the forward- and backward-time FTLE of the photospheric velocity field at $t_0 =$ 2006 December 12 18:24 UT and $t_0 =$ 2006 December 12 22:24 UT, using the same integration time $|\tau| = 4$ hr. Figure 4 displays the repelling (green) LCS and aLCS (red) for two t_0, which form the "Lagrangian skeletons" of the photospheric turbulence.

Attracting and repelling LCSs act as barriers to particle transport. A material line is a smooth curve of fluid particles

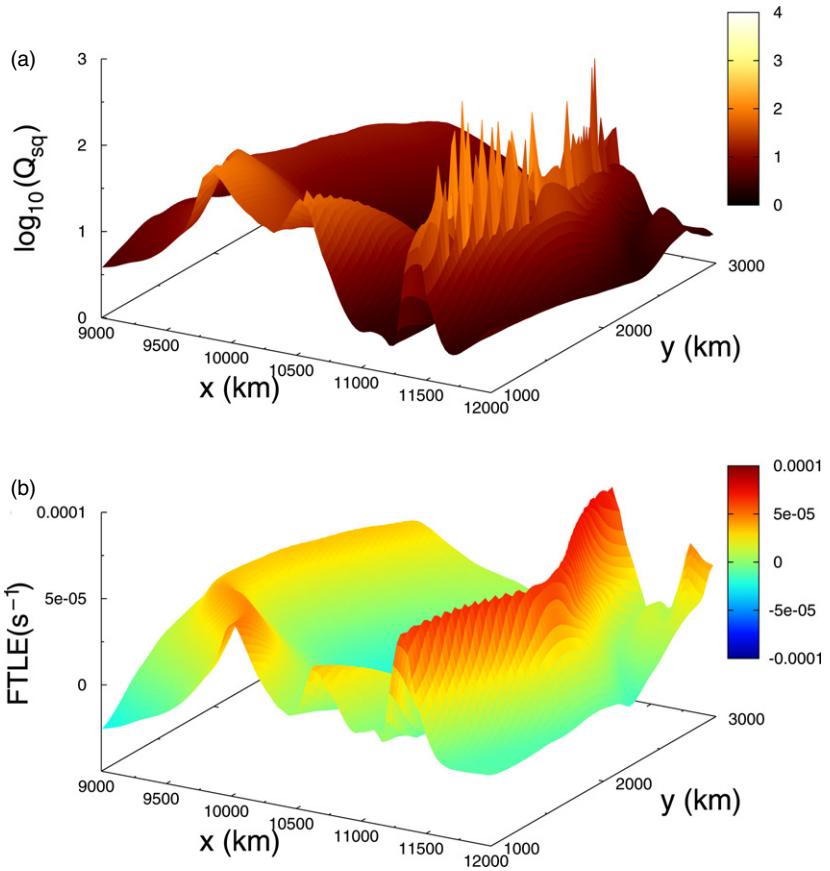

Figure 8. 3D plots of the squashing Q-factor and repelling LCS. (a) $\log_{10}(Q_{\rm sq})$; (b) f-FTLE for $t_0 =$ 2006 December 12 14:24 UT and $\tau = +12$ hr, corresponding to the rectangle regions indicated in Figure 7.

(A color version of this figure is available in the online journal.)

advected by the velocity field (Haller 2001). These attracting and repelling material lines are the analogues of stable and unstable manifolds of time-independent fields (Shadden et al. 2005; Shadden 2011). Numerical studies of 2D flows have elucidated the role of material lines (Haller & Yuan 2000; Miranda et al. 2013). The repelling material lines yield ridges in the maximum f-FTLE field and attracting material lines yield ridges in the maximum b-FTLE field (Rempel et al. 2012), as seen in Figures 3 and 4.

5. DISCUSSION AND CONCLUSIONS

In this paper, we showed that Eulerian coherent structures and LCSs give very different information of the dynamics and structure of astrophysical plasma flows. Eulerian coherent structures give instantaneous information of plasma dynamics and structure at a given time, whereas LCSs account for the integrated effect of plasma dynamics and structure in a finite-time interval. Arguably, instantaneous quantities may be considered inappropriate to understand inherently transient phenomena since such quantities may not properly convey the integrated behavior of constantly changing flow. LCSs typically account for such integrated behavior more naturally by considering the integrated fluid motion to reveal organizing flow features.

In the context of photospheric turbulence, we showed in Figure 1 that the Eulerian analysis is able to differentiate two types of coherent structures arising from either deformation or vorticity. An enlargement of the rectangle region indicated at Figure 1 at 2006 December 12 18:24 UT is depicted in Figure 5. The pattern of streamlines in Figure 5(a) identifies the localized region of a vortex in the photospheric flow. Figures 5(c) and (d) show that this vortex region is characterized by high values of the modulus of both deformation and vorticity. Figure 5(b) shows that the Q-criterion can differentiate clearly two subregions: the deformation Eulerian coherent structures (blue subregion) and the vortical Eulerian coherent structures (red subregion). For the sake of clarity, a corresponding 3D view of Figure 5 is presented in Figure 6. Our Eulerian analysis shows that, on average, in the plage region the deformation Eulerian coherent structures dominate over the vortical Eulerian coherent structures in the turbulent photospheric flows, as seen in Figure 2.

The Lagrangian analysis is able to provide further information of magnetic and velocity fields of the photospheric turbulence missing in the Eulerian analysis. Yeates et al. (2012) demonstrated that it is possible to make the link between the squashing Q-factor and the maximum Lyapunov exponent σ_1 of the repelling LCSs, since both quantities are similar measures of the local rate of stretching at a given point and defined by the norm of the Cauchy–Green tensor of the deformation imposed by the field-line mapping. Note, however, that there are some differences between these two quantities. While the squashing Q-factor uses the Frobenius norm of the tensor, σ uses the spectral norm; while the squashing Q-factor is dimensionless, σ has units of inverse time and includes the logarithm in its definition in Equation (5). The close similarity of these two quantities is shown in Figure 7, where the squashing Q-factor calculated for the same region of the photosphere under

study is shown in Figure 7(a) and the corresponding repelling LCSs are shown in Figure 7(b). Both Figures 7(a) and (b) are computed for $t_0 = 2006$ December 12 14:24 UT and $\tau = +12$ hr, the same as Figure 3(c). Figure 7(a) adopts the logarithmic scaling since certain trajectories typically become exponentially separated in time, which shows the emergence of thin ridges of high values of the squashing Q-factor representing the quasi-separatrix layers. These ridges are interspersed by regions of low values of the squashing Q-factor. Figure 7(b) shows the emergence of thin ridges of high positive values of σ_1, representing the locally strongest repelling material surfaces in the photospheric flow. These ridges are interspersed by regions of negative σ_1 that represent converging trajectories of the plasma transport. Evidently, the ridges of the quasi-separatrix layers in Figure 7(a) are co-spatial with the ridges of the photospheric flow in Figure 7(b). We wish to point out that the squashing Q-factor, denoted by Q_{sq}, is different from the Q-criterion denoted by Q as defined by Equation (1). Q_{sq} is related to the repelling LCSs and quasi-separatrix layers, whereas Q is the Okubo–Weiss parameter related to Eulerian coherent structures and not related to the maximum Lyapunov exponent σ_1 at all. For the sake of clarity, a 3D view of the rectangle regions of Figure 7 is presented in Figure 8. Note that the spiky features seen in Figure 8(a) may be related to numerical issues that can be smoothed by applying a refined numerical procedure (Pariat & Démoulin 2012). A recent combined study of QSL and Poincaré maps of a magnetic flux rope based on particle-in-cell simulations succeeded to identify regions of heating and current generation by magnetic reconnection (Restante et al. 2013).

As mentioned in Section 1, the Lagrangian analysis based on corks can provide insight into the relationship between magnetic fields and plasma flows in the photosphere. Roudier et al. (2009) used a two-day time sequence of *Hinode*/SOT data to study the relation between the photospheric horizontal flow and the magnetic field network in a region of quiet Sun containing four supergranules. They applied the cork technique to analyze the role of the tree of fragmenting granules in the passive advection of small-scale magnetic elements, and demonstrate that the final state is a patchy distribution of magnetic elements concentrated at the borders of supergranules related to photospheric downflows. Our technique of LCSs is closely related to corks, but gives additional important information missing in the cork-based studies as demonstrated below. Figure 9 shows a comparison of the line-of-sight magnetic field B_z measured by *Hinode*/SOT at $t = 2006$ December 13 02:24 UT (Figure 9(a), same as Figure 1) and the aLCSs computed for $t_0 = 2006$ December 13 02:24 UT and $\tau = -12$ hr (Figure 9(b), same as Figure 3(f)). It is possible to identify similar patterns in Figures 9(a) and (b). For example, a superposition of the rectangle regions marked in Figures 9(a) and (b) is shown in Figure 9(c) (where the thresholded b-FTLE with $\sigma_1 > 4 \times 10^{-5}$ is plotted), which shows clearly the proximity of the trajectory of plasma flows to the magnetic field, similar to the cork results of Roudier et al. (2009). In addition, Figure 9(b) shows the emergence of thin ridges of high positive values of σ_1, representing the locally strongest attracting material surfaces in the photospheric flow. These ridges are interspersed by regions of negative σ_1 that represent diverging trajectories of the plasma transport. For the sake of clarity, a 3D view of the rectangle regions of Figure 9 is presented in Figure 10.

In order to confirm the validity of Figures 9 and 10, we performed 3D numerical simulations of large-scale dynamos in turbulent compressible convection with uniform horizontal

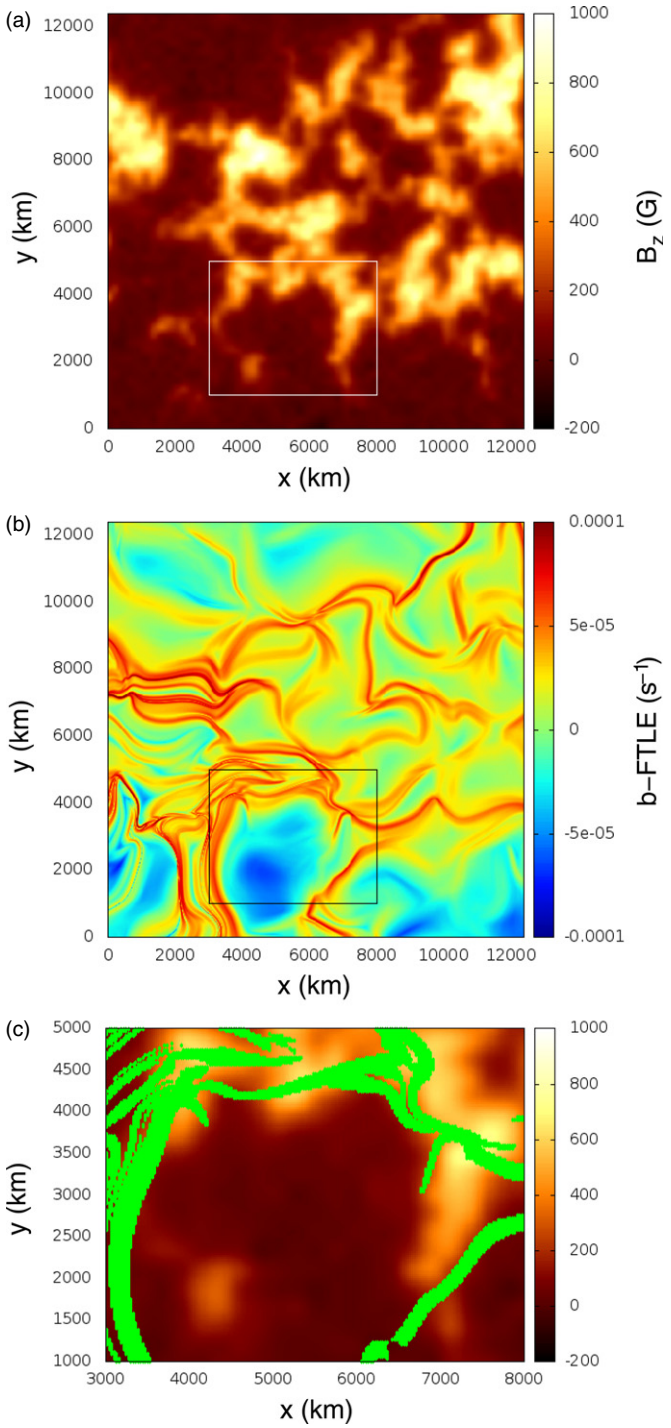

Figure 9. Comparison of the magnetic field and attracting LCS. (a) The line-of-sight magnetic field B at $t = 2006$ December 13 02:24 UT and (b) the b-FTLE for $t_0 = 2006$ December 13 02:24 UT and $\tau = -12$ hr. A superposition of the rectangle regions of (a) and (b) (green) is shown in (c), where the thresholded $\sigma_1 > 4 \times 10^{-5}$ is applied to b-FTLE.

(A color version of this figure is available in the online journal.)

shear and rotation. The dimensionless compressible magnetohydrodynamics equations are solved in a simulation box divided into three layers, an upper cooling layer, a convectively unstable layer, and a stable overshoot layer, with constant gravity in the vertical direction, as described by Käpylä et al. (2008). The box has dimensions $(L_x, L_y, L_z) = (8, 8, 2)d$, where d is the

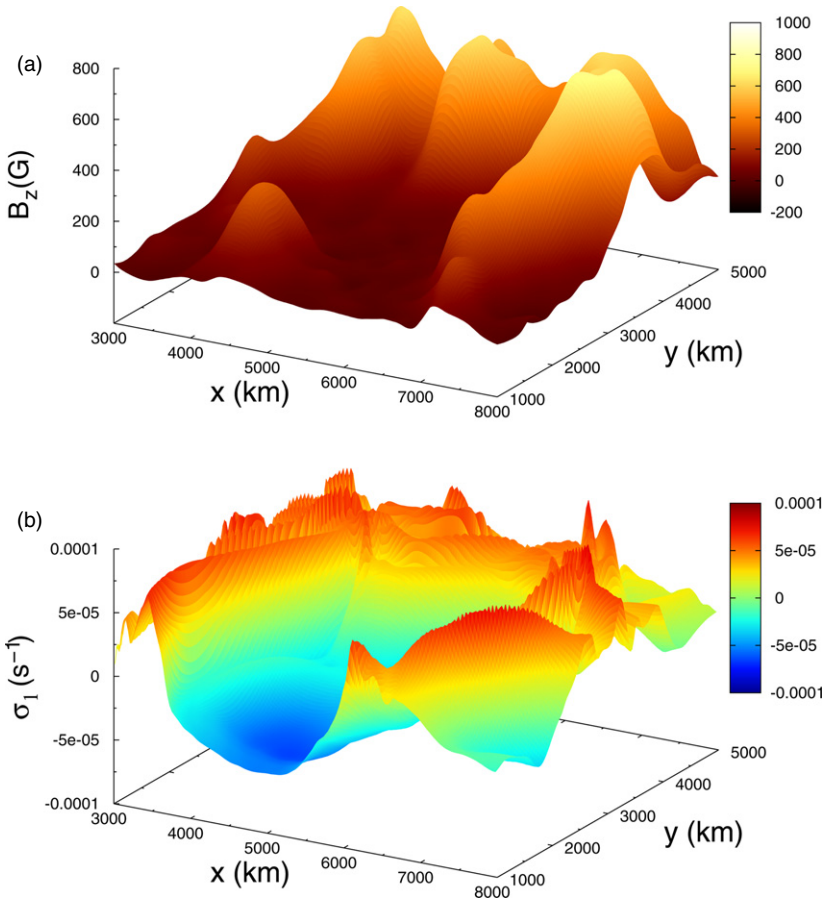

Figure 10. 3D plots showing the comparison of the magnetic field and attracting LCS. (a) The line-of-sight magnetic field B_z at $t =$ 2006 December 13 02:24 UT and (b) the b-FTLE for $t_0 =$ 2006 December 13 02:24 UT and $\tau = -12$ hr, corresponding to the rectangle regions indicated in Figures 9(a) and (b).
(A color version of this figure is available in the online journal.)

depth of the convectively unstable layer, and shearing periodic boundary conditions are used in the horizontal direction. In the vertical direction we use stress-free boundary conditions for the velocity field and vertical field conditions for the magnetic field. In our simulations we adopt dimensionless quantities, setting $d = \rho_0 = g = \mu_0 = 1$, where g is gravity, distance is in units of d, density in units of the initial value at the base of convective layer ρ_0, time in units of the free-fall time $\sqrt{d/g}$, velocity in units of $\sqrt{dg}$, and magnetic field in units of $\sqrt{d\rho_0\mu_0 g}$.

The physical parameters (e.g., kinematic viscosity, resistivity, heat conductivity, rotation velocity) are chosen to ensure the onset of a large-scale magnetic field in a moderately turbulent velocity field. For a detailed setup, we direct the reader to run D2 in Käpylä et al. (2008). The model is solved with the PENCIL CODE,[8] which employs sixth-order finite differences in space and third-order variable step Runge-Kutta integration in time.

Figure 11(a) shows a 2D image of the vertical component of the magnetic field B_z near the top of the convective layer at a time t_0 when the magnetic energy growth has already saturated. This figure shows that the simulated large-scale turbulent dynamo reproduces the pattern of convective cells, similar to granulations in the photosphere. In particular, it shows that the network of high concentration of magnetic flux is located in the boundaries between the convective cells, corresponding to the intergranular lanes. The elongated convective cells in Figure 11 result from the shear. Since there is an imposed large-scale flow in the y direction, it is expected that the convective cells would be elongated along this direction. This is more pronounced after a strong large-scale magnetic field develops due to the dynamo mechanism. Figure 11(b) shows the b-FTLE computed for the horizontal velocity field (v_x, v_y) at t_0 using $\tau = -10$ time units. The ridges of high values of b-FTLE in Figure 11(b) indicate the locations of converging plasma flows. In Figure 11(c) we plot the superposition of the thresholded b-FTLE (with $\sigma_1 > 0.1$) on top of B_z. For the sake of clarity, a 3D view of the rectangle regions of Figure 11 is given in Figure 12, where the modulus of B_z is plotted in comparison with the b-FTLE. Evidently, Figures 11 and 12 render support for the results of Figures 9 and 10 that there is correspondence of the network of high magnetic flux concentration to the aLCS in the photospheric velocity.

Our data analysis was based on one vertical component of magnetic field derived from the horizontal velocity, which may be restrictive in making predictions for comparisons with observations since the properties of 2D and 3D turbulence are qualitatively different. However, van Ballegooijen & Mackay (2007) showed that on the average the magnetic field is largely vertical at the photosphere; hence, it is expected that the properties of the turbulence are approximately 2D in certain regions of the photosphere. Physically, this is because we are dealing in this paper with plages at the photospheric level that are due to magnetoconvection at this layer, above which the medium is convectively stable. Observationally, this is confirmed by vector magnetograms showing that the magnetic field is more

[8] http://pencil-code.googlecode.com/

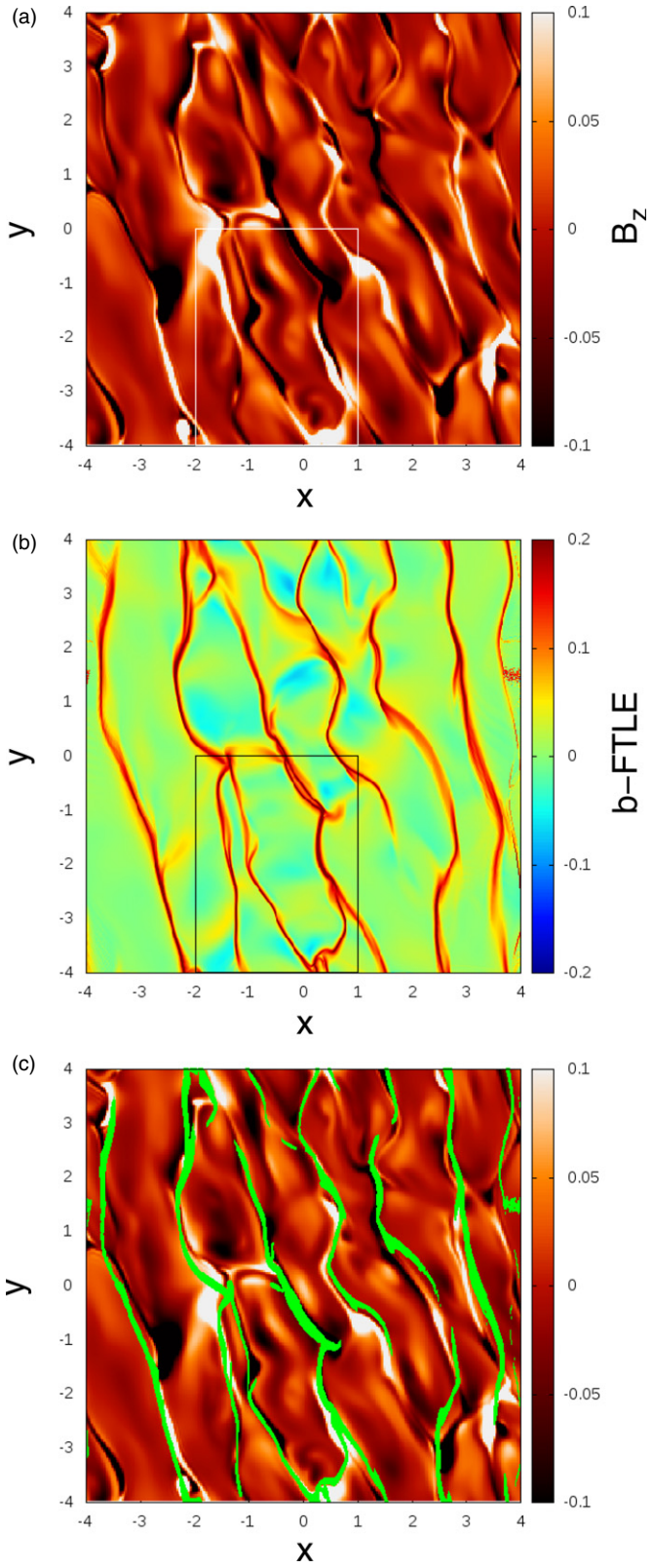

Figure 11. 2D plots of numerical simulation of compressible convection. (a) The vertical component of the magnetic field B_z at time t_0; (b) the b-FTLE computed at t_0 with $\tau = -10$ time units; (c) a superposition of (a) and (b) (green), where the threshold $\sigma_1 > 0.1$ is applied to b-FTLE.

(A color version of this figure is available in the online journal.)

vertical in the plage regions where B is strong (Bommier et al. 2007). There is horizontal magnetic field over the granules and in the polar region. The technique of reconstruction of horizontal velocity from the vertical magnetic field first introduced by Chae (2001) has become a standard means to analyze the photospheric data. A comparison of the performance of several methods for the velocity inversion from time series of photospheric vector magnetograms was carried out by Welsch et al. (2007). In regard to FTLE, we are not necessarily interested in obtaining exact predictions of the Lyapunov exponent; rather, we are interested in revealing LCS. It is LCS that can be directly compared with physical observations, not FTLE values. With that in mind, the question becomes whether or not locations of dominant stretching (the LCS locations) can be observed from advecting with the horizontal flow. In most cases the answer is yes, because while the strain value will generally change if advected in the full 3D flow, the locations of maximal strain are less likely to change (if the plasma were most highly stretched in the z-direction, this would directly contradict the quasi-2D assumption). 3D effects become increasingly important as integration time is increased. Initially the dominant structures will be captured in the 2D analysis, but further increases in integration time will generally produce finer scale mixing in 3D that is not possible in 2D. Particles have greater propensity to mixing in 3D, leading to finer scale structures as integration time increases, but dominant separation patterns will hold in 2D analysis. This behavior has been observed in many different applications of LCS. Note that the Q-criterion does not provide information about the temporal structure of the underlying turbulence, whereas FTLE incorporates both the spatial and temporal structures in that it evaluates the integrated effect of the flow on flow topology. We have demonstrated possible techniques for analyzing photospheric flows, in particular, we have elucidated the importance of LCSs. In order to determine how these techniques contribute to providing new information on the nature of the photospheric flows, further analysis of a large number of quiet and active regions of the photosphere and numerical simulations are required. Future works should (1) study the relation between the pdf of Q-criterion and the turbulence spectrum, (2) find out if the Q-criterion is skewed in all regions in the photosphere, and (3) address the effect of the vertical velocity in Eulerian coherant structures and LCSs.

In conclusion, we extended the observational study by Yeates et al. (2012) of LCSs in the photospheric velocity to show that in addition to the correspondence of the network of quasi-separatrix layers in the repelling LCS demonstrated by Yeates et al. (2012), there is a correspondence of the network of high magnetic flux concentration to the aLCS in the photospheric flows, confirmed by both observations and numerical simulations. Hence, the repelling and aLCSs of the photospheric velocity provide complementary information of the local dynamics and topology of solar magnetic fields. Although the corks coincide with the network of magnetic flux, they are not the best way to find the transport barriers and the directions of the flow convergence. We showed that the aLCSs are more suitable for these tasks because they trace continuous curves (material lines) that are the explicit structures potentially responsible for observed physical patterns and at the same time measure the local rate of contraction/expansion in the flow. While Eulerian coherent structures provide useful insights of the snapshot of the photospheric flows, they fail to reveal the fine structures of the transport barriers and the local dynamics of the flows that are readily provided by the repelling and aLCSs.

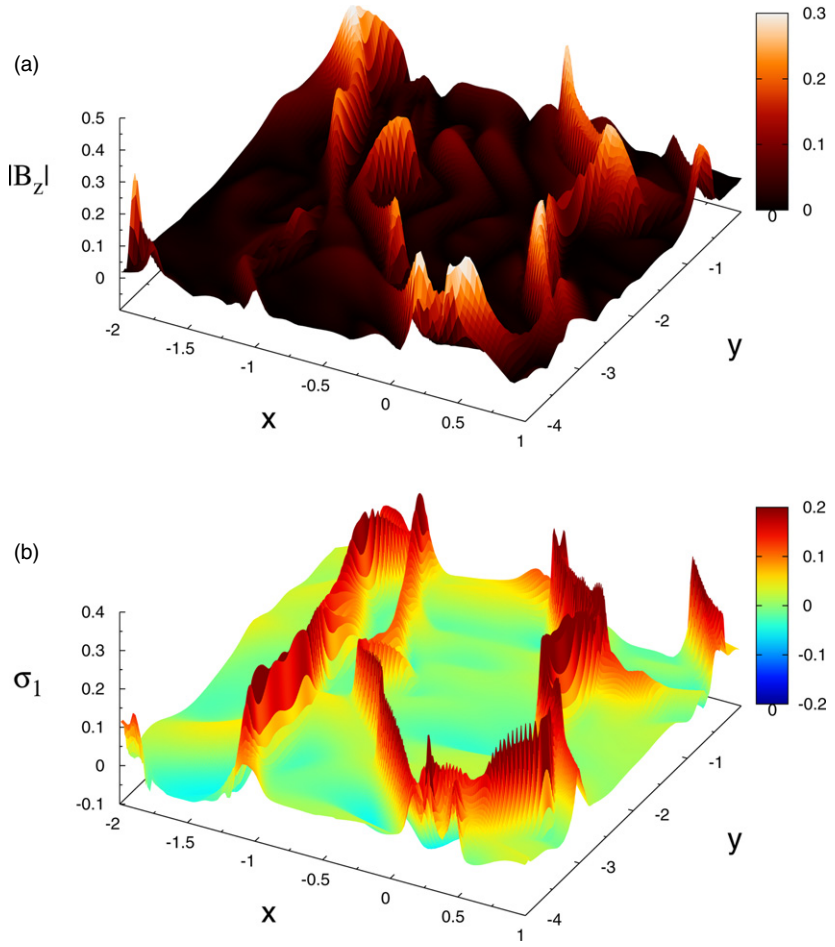

Figure 12. 3D plots of numerical simulation of compressible convection corresponding to the rectangle regions indicated in Figures 9(a) and (b). (a) Modulus of the vertical component of the magnetic field B_z at time t_0; (b) the b-FTLE for t_0 and $\tau = -10$ time units.

(A color version of this figure is available in the online journal.)

A.C.L.C. acknowledges the support of CNPq, the award of a Marie Curie Fellowship by the European Commission, and the hospitality of Paris Observatory. E.L.R. acknowledges the financial support of CNPq (Brazil) and Sâo Paulo Research Foundation (FAPESP) under grant 2013/22314-7. We thank Petri Käpylä for providing the configuration files for the PENCIL CODE MHD simulations. The authors are grateful to the referee for valuable comments that led to the improvement of discussions.

REFERENCES

Abramenko, V. I., Carbone, V., Yurchyshyn, V., et al. 2011, ApJ, 743, 133
Arzani, A., & Shadden, S. C. 2012, PhFl, 24, 081901
Beron-Vera, F. J., Olascoaga, M. J., & Goni, G. J. 2010, JPO, 40, 2466
Bommier, V., Landi Degl'Innocenti, E., Landolfi, M., & Molodij, G. 2007, A&A, 464, 323
Bonet, J. A., Márquez, I., Sánchez Almeida, J., et al. 2010, ApJL, 723, L139
Bonet, J. A., Márquez, I., Sánchez Almeida, J., Cabello, I., & Domingo, V. 2008, ApJL, 687, L131
Borgogno, D., Grasso, D., Pegoraro, F., & Schep, T. J. 2011, PhPl, 18, 102307
Brandenburg, A., Jennings, R. L., Nordlund, Å., et al. 1996, JFM, 306, 3
Cadavid, A. C., Lawrence, J. K., Christian, D. J., Jess, D. B., & Mathioudakis, M. 2012, in ASP Conf. Ser. 463, The Second ATST-EAST Meeting: Magnetic Fields from the Photosphere to the Corona, ed. T. Rimmele, A. Tritschler, F. Wöger et al. (San Francisco, CA: ASP), 75
Cadavid, A. C., Lawrence, J. K., & Ruzmaikin, A. A. 1999, ApJ, 521, 844
Chae, J. 2001, ApJL, 560, L95
Del Moro, D., Giordano, S., & Berrilli, F. 2007, A&A, 472, 599
Démoulin, P., Henoux, J. C., Priest, E. R., & Mandrini, C. H. 1996, A&A, 308, 643
Haller, G. 2001, PhyD, 149, 248
Haller, G., & Yuan, G. 2000, PhyD, 147, 352
Hasan, S. S., & van Ballegooijen, A. A. 2008, ApJ, 680, 1542
Hunt, J. C. R., Wray, A. A., & Moin, P. 1988, Eddies, Streams, and Convergence Zones in Turbulent Flows, Center for Turbulence Research Report CTR-S88 http://ctr.stanford.edu/Summer/201306111537.pdf
Käpylä, P. J., Korpi, M. J., & Brandenburg, A. 2008, A&A, 491, 353
Kitiashvili, I. N., Kosovichev, A. G., Mansour, N. N., & Wray, A. A. 2012, ApJL, 751, L21
Kitiashvili, I. N., Kosovichev, A. G., Wray, A. A., & Mansour, N. N. 2010, ApJ, 719, 307
Lawrence, J. K., Cadavid, A. C., Christian, D. J., Jess, D. B., & Mathioudakis, M. 2011, ApJL, 743, L24
Lawrence, J. K., Cadavid, A. C., Ruzmaikin, A. A., & Berger, T. E. 2001, PhRvL, 86, 5894
Lawrence, J. K., & Schrijver, C. J. 1993, ApJ, 411, 412
Lehahn, Y., d'Ovidio, F., Lévy, M., Amitai, Y., & Eyal Heifetz, E. 2011, GeoRL, 39, L16610
Leoncini, X., Agullo, O., Muraglia, M., & Chandre, C. 2006, EPJB, 53, 351
Lepreti, F., Carbone, V., Abramenko, V. I., et al. 2012, ApJL, 759, L17
Miranda, R. A., Rempel, E. L., Chian, A. C.-L., et al. 2013, Chaos, 23, 033107
Padberg, K., Hauff, T., Jenko, F., & Junge, O. 2007, NJPh, 9, 400
Pariat, E., & Démoulin, P. 2012, A&A, 541, A78
Peng, J., & Peterson, R. 2012, AtmEn, 48, 230
Polygiannakis, J. M., & Moussa, X. 1996, SoPh, 166, 423
Rempel, E. L., Chian, A. C.-L., & Brandenburg, A. 2011, ApJL, 735, L9
Rempel, E. L., Chian, A. C.-L., & Brandenburg, A. 2012, PhyS, 86, 018405
Rempel, E. L., Chian, A. C.-L., Brandenburg, A., Muñoz, P. R., & Shadden, S. C. 2013, JFM, 729, 309
Restante, A. L., Markidis, S., Lapenta, G., & Intrator, T. 2013, PhPl, 20, 082501

Rondi, S., Roudier, Th., Molodij, G., et al. 2007, A&A, 467, 1289
Roudier, T., Svanda, M., Meunier, N., et al. 2008, A&A, 480, 255
Roudier, Th., Rieutord, M., Brito, D., et al. 2009, A&A, 495, 945
Sapsis, T., & Haller, G. 2009, JAtS, 66, 2481
Schmieder, B., Roudier, T., Mein, N., et al. 2013, A&A, in press
Schrijver, C. J., Zwaan, C., Balke, A. C., Tarbell, T. D., & Lawrence, J. K. 1992, A&A, 253, L1
Shadden, S. C. 2011, in Transport and Mixing in Laminar Flows: From Microfluids to Oceanic Currents, ed. R. Grigoriev (Germany: Wiley VCH), chap. 3
Shadden, S. C., Lekien, F., & Marsden, J. E. 2005, PhyD, 212, 271
Shadden, S. C., & Taylor, C. A. 2008, Ann. Biomedical Eng., 36, 1152
Shelyag, S., Keys, P., Mathioudakis, M., & Keenan, F. P. 2011, A&A, 526, A5
Simon, G. W., Title, A. M., Topka, K. P., et al. 1988, ApJ, 327, 964
Simon, G. W., & Weiss, N. O. 1989, ApJ, 345, 1060
Solanki, S. 1993, SSRv, 63, 1
Stein, R. F., & Nordlund, A. 1998, ApJ, 499, 914
Steinberg, A. M., & Driscoll, J. F. 2009, CoFl, 156, 2285
van Ballegooijen, A. A., & Mackay, D. H. 2007, ApJ, 659, 1713
van Ballegooijen, A. A., Nisenson, P., Noyes, R. W., et al. 1998, ApJ, 509, 435
Welsch, B. T., Abbett, W. P., DeRosa, M. L., et al. 2007, ApJ, 670, 1734
Welsch, B. T., Fisher, G. H., Abbett, W. P., & Regnier, S. 2004, ApJ, 610, 1148
Welsch, B. T., Kusano, K., Yamamoto, T. T., & Muglach, K. 2012, ApJ, 747, 130
Yeates, A. R., Hornig, G., & Welsch, B. T. 2012, A&A, 539, A1